nature communications

Article

https://doi.org/10.1038/s41467-024-51088-0

Unassisted photoelectrochemical CO_2-to-liquid fuel splitting over 12% solar conversion efficiency

Received: 6 July 2023

Accepted: 29 July 2024

Published online: 14 August 2024

Check for updates

Bilawal Khan[1], M. Bilal Faheem[2], Karthik Peramaiah[3,4], Jinlan Nie[5], Hao Huang[4], Zhongxiao Li[1], Chen Liu[4], Kuo-Wei Huang[3,4] & Jr-Hau He[1]

The increasing need to control anthropogenic CO_2 emissions and conversion to fuels features the necessity for innovative solutions, one of which is photoelectrochemical system. This approach, capable of yielding gaseous production progressively, is facing challenges for liquid fuels generation due to optical, electrical, and catalytic properties. This study employs a standalone photoelectrochemical setup, in which InGaP/GaAs/Ge photoanode is integrated with tin-modified bismuth oxide cathode to convert CO_2 into liquid formic acid. In unassisted two-electrode assembly, setup exemplifies its operational durability for 100 h, during which it maintains an average Faradaic efficiency of 88% with 17.3 mmol L^{-1} h^{-1} of yield, thereby excelling in average solar-to-fuel conversion efficiency at 12% with 60% of electrical energy efficiency under one sun illumination. This significant performance is further associated with metal-semiconductor interface formation between tin and bismuth oxide, which bridges electronic structures and generates an electric field at their interfaces. This study outperforms conventional solar-driven systems in operational durability and liquid fuel production.

Growing atmospheric CO_2 concentrations, the primary contributor to global warming, pose significant challenges[1,2]. Projections indicate that, without intervention, anthropogenic CO_2 levels could approach ~590 ppm, potentially triggering an average temperature rise of +1.9 °C by this century[3]. Numerous renewable strategies have been implemented to mitigate surplus CO_2 emissions, including recycling, capturing, and conversion; however, their practical integration faces challenges to control excessive CO_2 re-emission and implement complicated systems[4–7]. Among those, photoelectrochemical CO_2 reduction reaction (PEC-CO_2RR) systems, known as artificial photosynthesis, present a viable strategy to convert solar energy into value-added by-products[8–10]. Among those, high-energy density liquid by-products, such as formic acid (HCOOH), are advantageous owing to ease of storage, transportation, separation, and displacement at peak volumetric densities[5,11]. Nevertheless, the investigation into solar-assisted CO_2-converted liquid productions remains inadequate, primarily due to selectivity, sub-optimal yields, limited conversion efficiency and operational durability[5,12].

Among reported solar-driven systems, PEC assemblies, synergistically coupled with catalyst layers, can efficiently catalyze CO_2 into valuable carbon-based high-energy density fuels[9,10]. Considering PEC as a significant configuration, several studies on dual-photoelectrode configurations have been reported to initiate the CO_2RR[5,13,14]. Conversely, a single-photoelectrode system that mimics artificial photosynthesis and is distinguished as a viable and economical alternative for efficient fuel synthesis is rarely investigated in PEC-CO_2RR due to

[1]Department of Materials Science and Engineering, City University of Hong Kong, Kowloon 999077, Hong Kong. [2]Department of Mechanical and Aerospace Engineering, Syracuse University, Syracuse, NY 13244, USA. [3]Agency for Science, Technology, and Research, Institute of Sustainability for Chemicals, Energy and Environment, 1 Pesek RoadJurong Island Singapore 627833, Singapore. [4]KAUST Catalysis Center and Division of Physical Science and Engineering, King Abdullah University of Science and Technology, Thuwal 23955-6900, Saudi Arabia. [5]School of Physics, University of Electronic Science and Technology of China, 610054 Chengdu, China. e-mail: jrhauhe@cityu.edu.hk

the limited power output[15,16]. This single-photoelectrode PEC assembly facilitates CO_2 conversion beyond conventional structures by effectively mitigating charge carrier transport losses and thermodynamic inefficiencies, such as heat transfer between electrodes[17]. However, this single-photoelectrode setup either necessitates external bias or drives a half-reaction without applied bias due to the low power output generated by photoelectrode[17–19]. Therefore, a lack of evidence reveals the ability of a single-photoelectrode design to catalyze the bias-free PEC-CO_2RR, thereby limiting the potential stride towards unbiased operation[20].

In addition to the above considerations, selecting a single-photoelectrode with a tandem configuration capable of producing sufficient power output is significant for driving PEC-CO_2RR without external energy input[21]. The tandem structures reported to date are mainly pertinent to efficient carbon monoxide (CO) or syngas productions, and yet, catalyzing liquid fuels with high η_{STF}, selectivity, and long-run yields remains a prominent concern[13,14,20,22,23]. Despite the efficient power output generation, the instability of photoelectrodes within aqueous solutions remains a significant challenge that impedes long-run operation[8]. This need arises to incorporate efficient protective layers against photocorrosion and chemical instability under aqueous environmental conditions, thereby prolonging operational durability[24]. Subsequently, highly active and low-onset potential electrocatalysts are prerequisites to maintain selectivity and yields for liquid fuels during long-run operation. Bismuth(Bi)-based electrocatalysts have gained prominence to convert CO_2 into HCOOH, primarily due to their exceptional catalytic performance and advantageous properties in stabilizing $CO_2^{\bullet-}$ intermediate[25,26]. However, low current density, less electrical conductivity, limited CO_2 adsorption capability, and inadequate selectivity at a more negative potential necessitate an interfacial engineering strategy for heterostructure design to modulate the electronic structure for performance improvement[27,28]. Hence, using an interfacial engineering approach to create metal-semiconductor interfaces, where differences in work functions between the metal and semiconductor enable charge transfer and adjust semiconductor band positions, is significant[29]. In metal-semiconductor interaction, metal components play a significant role in fine-tuning the composite's electronic structure[28]. Such interactions lead to orbital rehybridization and charge transport across the metal-support interface, inducing new chemical bond formation and molecular energy level adjustment[28,30]. This process adjusts the d-band structure of metals, enhancing the adsorption of reaction intermediates, thus lowering the energy barriers and facilitating the rate-limiting steps[30,31]. Additionally, metal-semiconductor interactions contribute to the stability of metal atoms on the support material through the formation of thermodynamically favorable metal-support bonds and promote charge redistribution via electron transfer[28,30]. Considering HCOOH yield as a major product, the synergistic interaction between semiconducting bismuth oxide (Bi_2O_3)-based catalysts with appropriate metal-based catalysts is a favorable choice for designing binary components to promote efficient and long-run CO_2 conversion[32–34]. To address these challenges, the fabrication of tandem-structured photoelectrode with optimal power output and low-onset potential catalyst is a viable choice for converting CO_2 into high-energy density liquid fuels.

This study implemented an unassisted PEC-CO_2RR setup using 3-J photoanode and Sn-modified Bi_2O_3 nanocomposites (NCs) to convert CO_2 to liquid HCOOH. During three-electrode configuration, the Sn-Bi_2O_3||3-J|Ni/RuO_x PEC device recorded an average FE of 90% with 19.7 mmol L^{-1} h^{-1} yield, resulting in significant η_{STF} of 15% and electrical energy efficiency (η_{EE}) of 57% for 100 h. The engineered Sn-Bi_2O_3 catalyst outperforms in CO_2 conversion rate due to electronic structure modulation at their interfaces. Theoretical density of states (DOS) findings further indicate that incorporating Sn with Bi_2O_3 upshifts the Fermi level. These upshifts in the Fermi level result in a stronger binding affinity of the catalyst towards the OCHO*, which enhances HCOOH formation. These observed effects are associated with enhanced CO_2 and OCHO* adsorption capabilities at the catalyst interface. Compared to the Bi_2O_3, the Gibbs free energy further confirms a reduction in formation energy on the Sn-Bi_2O_3 surface, confirming changes in the electronic structure after Sn modification. These insights facilitate PEC assembly and catalyst designs to synthesize high-energy density liquid fuels for scalable operations.

Results

Photoelectrode design, photovoltaic characteristics and devised assembly

In solar-driven reactions, the efficiency of the photoelectrode emerges as a critical determinant of overall performance. However, the most reported photoelectrodes incite severe charge recombination owing to their inherent photovoltage limitations and inadequate passivation layers, ultimately decreasing the efficacy[35,36]. The 3-J photoanode with a sufficient power output that can catalyze the CO_2RR without external bias is utilized in this study. At first, the rear side of the 3-J photoanode is integrated with Nickel (Ni)-foil, which serves dual purposes—stabilizing the device against photocorrosion and functioning as an efficient heat dissipation layer to perform PEC-CO_2RR under aqueous conditions[37]. This layer ensures the 3-J photoanode bottom and Ni interface an ohmic contact, unlike the Schottky barrier or anolyte-induced depletion layer over the Ni surface[38]. To fulfill the photovoltage prerequisites of PEC-CO_2RR, low-onset potential ruthenium oxide (RuO_x) is further deposited over the Ni-foil to catalyze the water oxidation at a low applied potential. This 3-J|Ni/RuO_x design of the PEC cell presents the distinct advantage of effectively decoupling the optical absorption and electrocatalytic interfaces, extending its longevity and operational range (Fig. 1a).

The photovoltaic characteristics of the 3-J photoanode under dry conditions were analyzed under AM 1.5 G illumination to validate the photovoltage requirements for PEC-CO_2RR. The performance metrics of the 3-J photoanode, as indicated by the current–voltage (*J–V*) profile, including open-circuit voltage (V_{OC}) of 2.6 V, a short-circuit current density (J_{SC}) of 13.97 mA cm^{-2}, a fill factor of 83.5%, and a power conversion efficiency standing at 29.8% (Fig. 1c). The *J–V* outcomes confirm that the photovoltages generated by 3-J photoanode surpass the potential requirements of PEC-CO_2RR (~2.2 eV, see Fig. 2a). To illustrate the light-absorption properties further and describe the integral role of 3-J photoanode in PEC performance, external quantum efficiency (EQE) with the absorption edge of each constituent sub-cell was evaluated (Fig. 1d). The uppermost sub-cell (GaInP, E_g = ~1.85 eV) exhibits efficient photon absorption within the 300–600 nm λ spectrum. Subsequently, photons that traverse the upper layer and reach the middle sub-cell (GaAs, E_g = ~1.40 eV) are absorbed within the 600–900 nm λ spectrum. Finally, the lowermost sub-cell (Ge, *Eg* = ~0.67 eV) captures high-frequency photons within the λ spectrum within the 900–1800 nm spectrum. The consistency between these EQE calculations and the J_{SC} values reveals the sufficient light-harvesting and effective charge carrier separation capabilities of the 3-J photoanode. Subsequently, using elemental mapping, the layered structure of the 3-J photoanode was confirmed with high-angle annular dark field scanning transmission electron microscopy (HAADF-STEM). With a structural composition incorporating semiconductors such as InGaP, GaAs, Ge, and layers coated with Ni and RuO_x, the cumulative thickness of the device was estimated to be ~6.2 µm. The illuminated surface of the 3-J photoanode was precisely characterized via TEM further, which presents numerous quantum wells distribution within the mediating region (Fig. S1). In terms of elemental dispersion, a ~500 nm thick layer of InGaP resides at the bottom structure, succeeded by a substantial ~5 µm thick layer of GaAs, interspersed with multiple quantum wells in the intermediary region, and concluded by a ~400 nm thick layer of Ge at the top, as elucidated in Fig. 1b.

https://doi.org/10.1038/s41467-024-51088-0

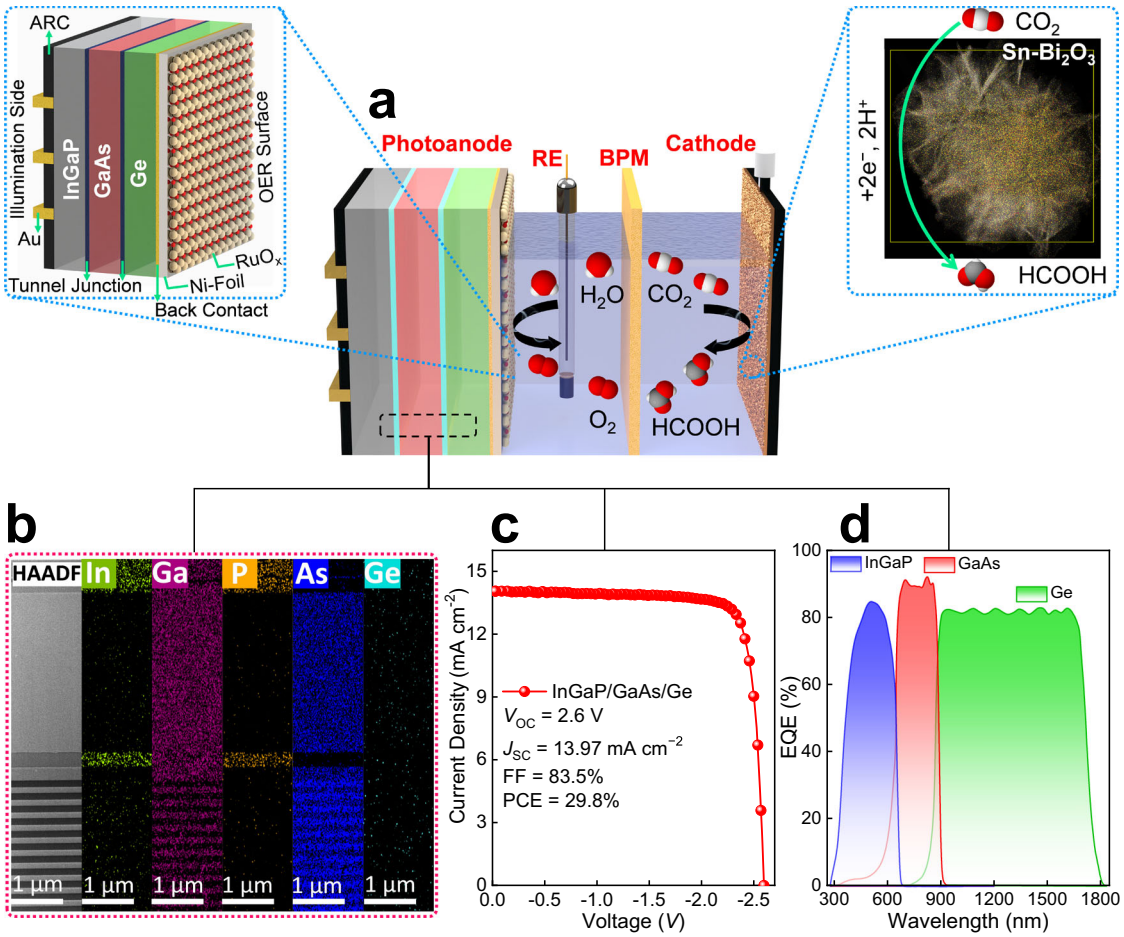

Fig. 1 | Schematics of the PEC assembly for CO_2-to-liquid fuel conversion and photovoltaic characteristics of the 3-J photoanode. a Mechanistic demonstration of the CO_2R_{cat}||3-J|Ni/RuO_x PEC device during CO_2RR; enlarged view of 3-J|Ni/RuO_x photoanode on the right-hand side and HAADF-STEM mapping of CO_2R_{cat} ($Sn\text{-}Bi_2O_3$) on the left-hand side. **b** HAADF-STEM of 3-J photoanode with elemental mapping of In, Ga, P, As, and Ge, with 1 μm size, respectively. **c** Operating current-voltage characteristics, and (**d**) EQE% of the 3-J photoanode. ARC: Anti Reflection Coating, RE: Reference electrode (Ag/AgCl), BPM: Bi-polar membrane.

In addition to the above considerations, an efficient, stable, and cost-effective system is a prerequisite for efficient PEC performance. To address this, an artificial photosynthesis-inspired, unassisted, two-electrode PEC-CO_2RR setup employing a single photoelectrode to catalyze both the cathodic reduction and anodic oxidation is devised. Figure 1a elucidates the schematics insights of the unassisted PEC-CO_2RR assembly, comprising 3-J|Ni/RuO_x photoanode with $Sn\text{-}Bi_2O_3$ (CO_2R_{cat})-cathode. The photogenerated electrons of the 3-J photoanode drift towards the front collection point, which is directly connected to the $Sn\text{-}Bi_2O_3$-cathode (separated by the bipolar membrane) to initiate CO_2RR, and holes transfer to the rear side of the photoanode on the Ni/RuO_x to facilitate water oxidation. Moreover, the physical representation of this PEC-CO_2RR setup is further depicted in Fig. S2.

Photoelectrochemical CO_2 reduction

The bias-free PEC system, operated by a single-photoelectrode, exemplifies a promising, cost-effective, and efficient approach to upscaling energy conversion processes. During PEC operation, the current-voltage characteristics of the 3-J|Ni/RuO_x photoanode (red) under 1-sun illumination with the electrochemically activated currents: anodic RuO_x (black) and cathodic $Sn\text{-}Bi_2O_3$ (green) under dark in aqueous conditions are measured first as displayed in Fig. 2a. Here, the red-green intersection curve of $Sn\text{-}Bi_2O_3$ signify the operating point for CO_2R at −0.73 V vs RHE and 12.99 mA cm^{-2} current density. Similarly, a potential of 1.46 V vs RHE is required to initiate water oxidation (indicated by the red-black intersection of RuO_x). Additionally, the PEC system experiences external voltage losses of ~0.4 V due to the bipolar membrane, as detailed in Supplementary Note 1 and Figs. S4–S5. Considering this, the PEC-CO_2RR necessitates ~2.59 V to derive the complete PEC-CO_2RR.

During PEC-CO_2RR, liquid HCOOH was a major product and gaseous H_2 (Supplementary Note 2) was analyzed as a minor product. Before PEC operation, 3-J|Ni/RuO_x photoanode in 0.5 M aqueous KOH (pH ~14) anolyte with CO_2-saturated CO_2R_{cat} in a 0.5 M aqueous potassium bicarbonate ($KHCO_3$) (pH ~7.4) catholyte was immersed separately. Within the three-electrode PEC-CO_2RR setup, the potential at the counter electrode ($Sn\text{-}Bi_2O_3$) was recorded first, where the system stabilized 0.25 V potential for 100 h (Fig. S3a). On hourly three-electrode PEC-CO_2RR operation, the CO_2R_{cat}||3-J|Ni/RuO_x setup exhibited 94 ± 1.9% FE, corresponding to a significant production amount of 20.3 ± 1.3 mmol L^{-1} h^{-1} (Fig. S6). Subsequently, this PEC assembly stabilized an average 90 ± 2.1% FE with a consistent yield of 19.7 ± 1.7 mmol L^{-1} h^{-1} for 100 h (Fig. 2b). The hourly nuclear magnetic resonance (NMR) performance for HCOOH is quantified further to confirm the amount of obtained liquid products (Fig. S7). To stimulate artificial photosynthesis-inspired, unassisted two-electrode PEC setup was executed further to synthesize the storable and economically viable liquid fuel synthesis. Prior to unassisted PEC operation, the *J*–*V* characteristics of the 3-J|Ni/RuO_x photoanode in two-electrode configurations under standard AM 1.5 G illumination in aqueous

https://doi.org/10.1038/s41467-024-51088-0

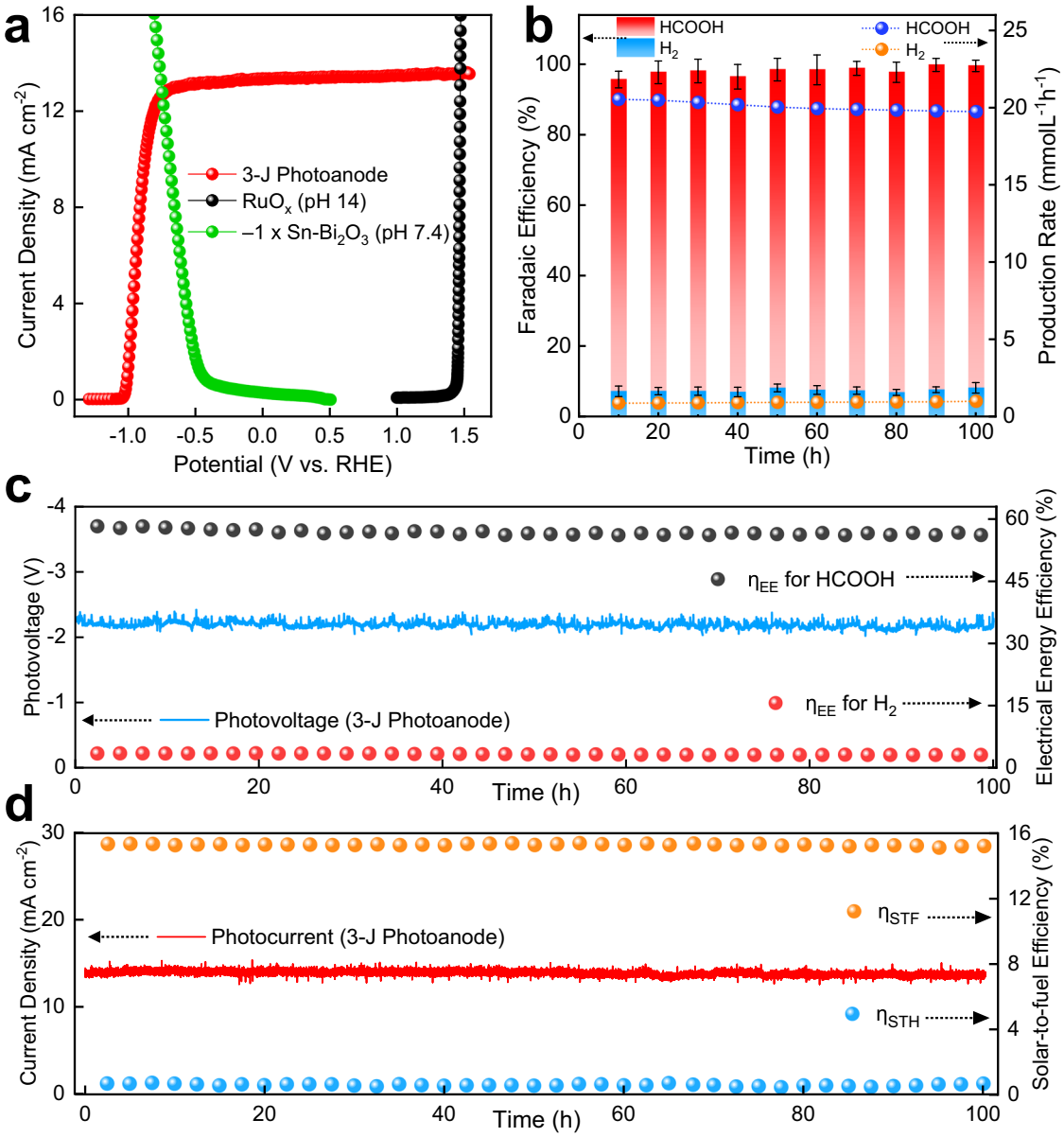

Fig. 2 | Three-electrode PEC-CO_2RR operation under AM 1.5 G illumination with CO_2R_{cat}||3-J|Ni/RuO_x PEC device. a Current–voltage characteristics of 3-J photoanode with electrochemically activated currents: anodic RuO_x with Ag/AgCl Reference Electrode and cathodic Sn-Bi_2O_3 NCs catalyst in the dark. **b** Calculated FE% (left-hand axis) and obtained HCOOH and H_2 production rates (right-hand axis) with Sn-Bi_2O_3 NCs cathode. The error bars indicate the results from ten individual tests. **c** Quantified Electrical Energy efficiency (η_{EE}%, right-hand axis) and operating photovoltages (left-hand axis) during 100 h of PEC-CO_2RR with 3-J photoanode and Sn-Bi_2O_3 cathode. **d** η_{STF}% of the cathodic products (right-hand axis) with the operating anodic photocurrent density (left-hand axis) during 100 h of PEC-CO_2RR using 3-J photoanode and Sn-Bi_2O_3 cathode. The setup recorded 2.14 ± 0.013 Ω resistance, and cell voltage readings have not been iR-corrected.

conditions were analyzed. In an unassisted two-electrode setup, this 3-J|Ni/RuO_x photoanode maintained a J_{SC} of 10.5 mA cm^{-2} (Fig. S8). Subsequently, in a two-electrode PEC-CO_2RR setup, the counter electrode (Sn-Bi_2O_3) recorded 0.25 V potential during long-run continuous operation of 100 h (Fig. S3b). In the initial hourly evaluation, the unassisted CO_2R_{cat}||3-J|Ni/RuO_x PEC device demonstrated 91 ± 2.3% FE with 17.9 ± 1.9 mmol L^{-1} h^{-1} product generation (Fig. S6). Subsequently, long-run 100 h of operation maintained a consistent FE of 88 ± 3.2% and delivered an average production of 17.3 ± 1.9 mmol L^{-1} h^{-1} (Fig. 3a). Additionally, the performance metrics of PEC-CO_2RR utilizing individual Ni-foil as an OER catalyst were assessed, and findings are thoroughly detailed in the Supplementary Note 3 and Figs. S9–11. Moreover, the half-anodic oxygen evolution reaction in both the three- and two-electrode configurations, occurring on the rear-side of the 3-J|Ni/RuO_x photoanode under AM 1.5 G illumination, are demonstrated in Supplementary Movie 1 and 2.

Electrical energy efficiency (η_{EE}), which reveals the energy difference during CO_2 conversion into targeted products, is a key factor for further scalability estimations is measured. Based on the obtained selectivity and generated photovoltage, CO_2R_{cat}||3-J|Ni/RuO_x PEC device demonstrated a remarkable average η_{EE} of 57.2 ± 1.5% for HCOOH during a three-electrode and 60.0 ± 1.9% with an unassisted two-electrode assembly during 100 h of PEC-CO_2RR (Figs. 2c, 3c). During 100 h of PEC-CO_2RR, the generation of photovoltages demonstrated a commendable consistency, thereby substantiating the stability of the PEC device within aqueous electrolytic conditions (Figs. 2c, 3c). These η_{EE} results confirm that an appropriate potential is crucial for targeting the desired products. In the PEC-CO_2RR, the η_{STF}

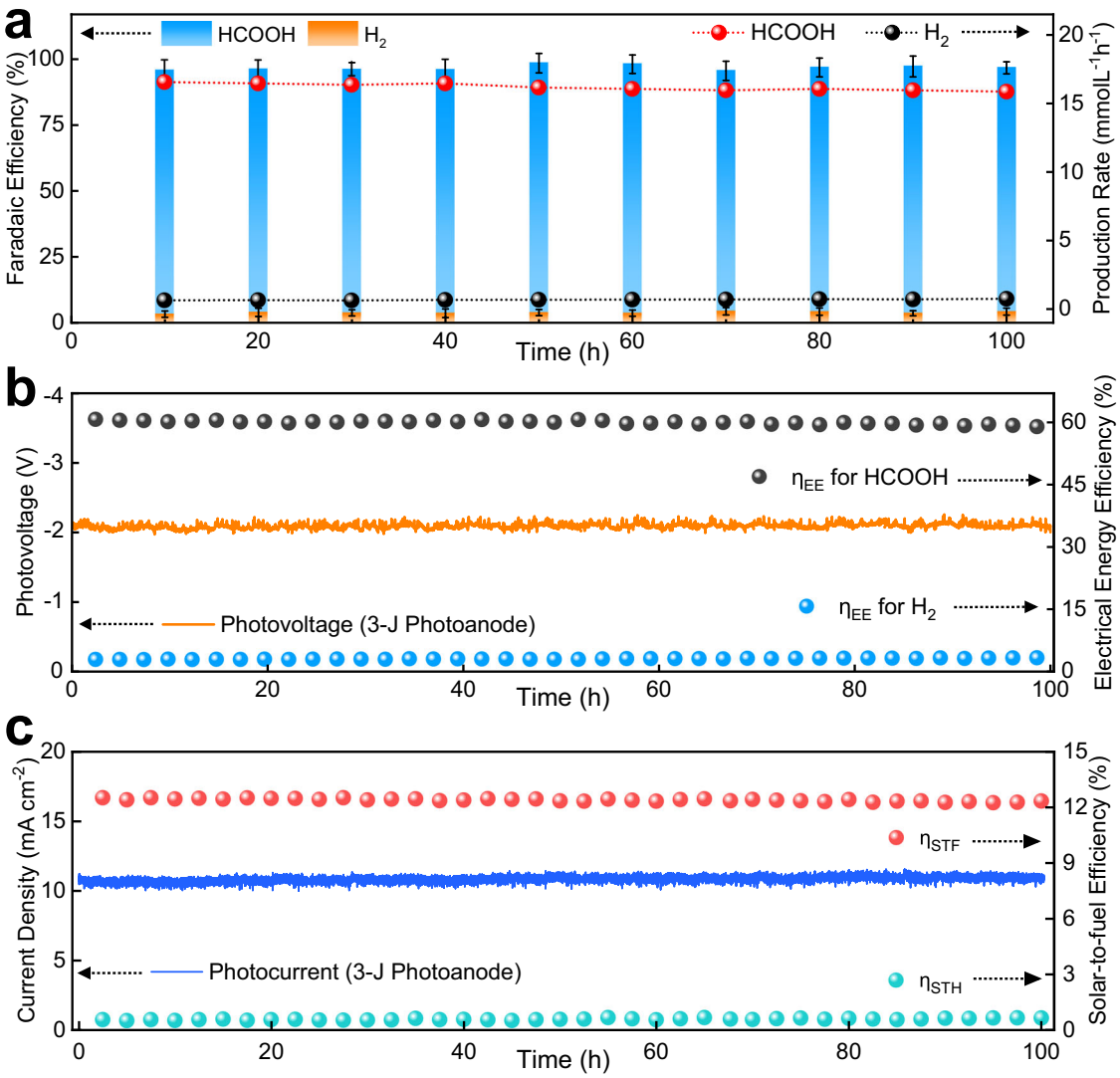

Fig. 3 | Two-electrode PEC-CO_2RR operation under AM 1.5 G illumination with CO_2R_{cat}||3-J|Ni/RuO_x PEC device. a Obtained FE% (left-hand axis) and production yields (mmol L^{-1} h^{-1}, right-hand axis) of HCOOH and H_2 using CO_2R_{cat}||3-J|Ni/RuO_x PEC device. The error bars indicate the results from ten separate measurements. **b** Calculated η_{EE}% (right-hand axis) and operating photovoltages (left-hand axis) during 100 h of PEC-CO_2RR with 3-J photoanode and Sn-Bi_2O_3 cathode. **c** η_{STF}% of the cathodic products (right-hand axis) and operating anodic photocurrent density (left-hand axis) during 100 h of PEC-CO_2RR using 3-J photoanode and Sn-Bi_2O_3 cathode. 3-E: Three-electrode, 2-E: Two-electrode. The setup recorded 2.14 ± 0.013 Ω resistance, and cell voltage readings have not been iR-corrected.

mark is state-of-the-art, indicating that the incident light induces the formation of the chemical bonds of various fuels. Based on obtained selectivity and photocurrent, CO_2R_{cat}||3-J|Ni/RuO_x PEC device in a three-electrode system exhibits remarkable η_{STF} of 15.5 ± 0.7% during hourly and recorded an average η_{STF} of 15.1 ± 0.9% for HCOOH throughout 100 h of experimentation (Fig. 2d). Operating under identical conditions, artificial leaf-inspired, unassisted two-electrode CO_2R_{cat}||3-J|Ni/RuO_x PEC device in hourly investigation recorded 12.5 ± 0.6% of η_{STF}, which was recorded at an average of 12 ± 0.9% during 100 h operation (Fig. 3d).

The lack of stability inherent to the photoelectrode represents a major challenge, effectively limiting the practical implementation of PEC devices. In the initial investigation, a 3-J photoanode without a protective layer (Ni-foil) was employed, which exhibited limited durability of <1 h within an aqueous electrolyte, thereby confirming its chemical instability and susceptibility to corrosion (Fig. S12). Consequently, the rear-side protected PEC device with Ni-foil demonstrated an enduring photocurrent for 100 h of CO_2R operation (Figs. 1e, 3c). Owing to the instability of the cathodic catalyst beyond 100 h in PEC-CO_2RR, the integrated 3-J|Ni/RuO_x photoanode with Pt-foil as a cathode was further experimented to validate its durability under aqueous circumstances. This individual PEC device exhibited robust operation over 500 h, with a negligible irreversible variation of 0.5% in photocurrent (Fig. S13). A slight deviation in the J–V characteristics under aqueous condition measurements was observed before and after 500 h of operation (Fig. S14). This indicates that the 3-J|Ni/RuO_x photoanode is durable for long-run experimentation. This exceptional performance confirms the Ni foil's efficient electrolyte permeation, thereby improving the chemical stability under aqueous conditions. Overall, passivation by integrating the Ni-foil as a protection layer efficiently maintains chemical stability, dissipating heat and preventing corrosion. Furthermore, using RuO_x as a low-onset potential catalyst effectively catalyzes water oxidation at a lower potential.

Significance of liquid-fuel and comparison analyses of PEC assembly

Among CO_2 converted liquid fuels, HCOOH is an exceptional choice due to its unique electron-per-mole advantage and high energy

density[39] Annually, ~800,000 metric tons of HCOOH are produced and employed in diverse applications, subsequently considered a remarkable H_2 storage medium due to rapid catalyst-aided dehydrogenation[40]. Its salient features in the liquid phase at ambient environmental conditions exhibit low toxicity and offer high H_2 storage volumetric density (approximately 53 g per litter)[40]. Inspired by artificial photosynthesis, PEC-CO_2 conversion into HCOOH is a compelling scheme for cost-effective commercial viability, given that the resulting liquid products can be precisely stored, seamlessly transported, and directly utilized[5,16,22]. Despite numerous PEC-CO_2RR-based gaseous generations, liquid fuel synthesis remains a significant concern due to high energy demands. Such systems consistently undergo several limitations, including inadequate photovoltages, chemical instability, high onset potential and catalyst durability constraints, thereby limiting these implementations on their road to commercial viability.

Considering PEC as a renewable method and HCOOH as a high-energy density liquid fuel, our research demonstrates a standalone bias-free CO_2R_{cat}||3-J|Ni/RuO_x device. Under AM 1.5 G illumination, unassisted CO_2R_{cat}||3-J|Ni/RuO_x PEC device, marked by high selectivity and long-run production yield, leads to significant η_{STF} over 100 h. Remarkably, the selectivity, operational durability, and recorded η_{STF} outperform those of previously reported photoanode- and photocathode-promoted PEC-CO_2RR setups (Table S1). The assembly, strategically segregating anodic and cathodic compartments within the PEC assembly, facilitates independent reaction adjustment further, thereby preventing the need for electrolyte flow, concentrated solar irradiance, gas-diffused photoelectrodes and thermoelectric systems[22,41]. The significant performance achieved in this work is credited to the multi-layered photoelectrodes design, which generates sufficient photovoltage, and the implementation of an artificial photosynthesis-inspired unassisted PEC assembly to induce bias-free CO_2RR. Progressing further on this achievement, catalyst selection and engineering emerge as crucial factors in long-run operations.

Electrochemical CO_2 reduction

To validate the selectivity, production yields and durability of cathode catalysts, the electrochemical performance was performed. The linear sweep voltammetry (LSV) of the cathode-catalysts (Bi_2O_3 and Sn-Bi_2O_3) revealed higher negative currents under CO_2 saturation than Argon, indicating strong interactions between CO_2 and electrode surfaces (Fig. S15a). Combining Sn (i.e., 1 to 4 wt.%) with Bi_2O_3 maximizes the current density, as LSV curves, selectivity, and production yields are presented in Fig. S16a, b and Table S2. With 3% Sn loading, the Sn-Bi_2O_3 demonstrated a FE of 95 ± 2.3% and 3.1 ± 1.2% with a yield rate of 20.7 ± 1.2 and 0.6 ± 0.8 mmol L^{-1} h^{-1} for HCOOH and H_2 at −0.73 V vs RHE potential, respectively (Fig. S15b). Under the same operation conditions, the Bi_2O_3 presented FE of 85 ± 1.7% and 5 ± 0.9% with a yield of 13.6 ± 1.1 and 1.4 ± 1.1 mmol L^{-1} h^{-1} for HCOOH and H_2, respectively (Fig. S15b). During 100 h of operation at −0.73 V vs RHE, the average FE of 90 ± 1.9% and 3.5 ± 1.3% with a production amount of 20.1 ± 1.2 and 0.7 ± 0.5 mmol L^{-1} h^{-1} corresponding to HCOOH and H_2 is achieved with Sn-Bi_2O_3, respectively. Moreover, the Bi_2O_3 performed an average of 80 ± 1.3% and 7.9 ± 1.1% FE with 11.9 ± 0.9 and 1.8 ± 0.8 mmol L^{-1} h^{-1} production relative to HCOOH and H_2, during 100 h of operation (Fig. S17). These enhancements in performance at a low applied potential and positive shift in onset potential are attributed to the appropriate loading of Sn onto Bi_2O_3. This considerable improvement primarily originates from the synergistic effects between the catalytically active sites of Bi and Sn. During this metal-semiconductor interface, the Sn facilitates electron transport to Bi_2O_3 at the interface, thereby increasing the number of active sites and stabilizing the reaction intermediates, thus improving the overall catalytic performance[33,42,43].

The hourly current densities in the −0.6 to −1.2 V vs RHE range with a decrease of −0.1 V in each run are further investigated (Fig. S18a, b). The Sn-Bi_2O_3 displays over 90 ± 2.5% FE towards HCOOH in the potential range from −0.7 to −1.1 V, which is restricted to ~82 ± 2.9% while utilizing the Bi_2O_3. This ultimate FE at a more negative potential is due to the enriched adsorption capacities of adsorbed $CO_2^{\bullet-}$ and OCHO*. Moreover, when the potential of −1.2 V is applied to the Sn-Bi_2O_3, the FE of HCOOH drops to 80 ± 3.8%, while that of H_2 improves to 18 ± 2.8%. Conversely, when a Bi_2O_3 NSs was employed, the FE for HCOOH decreased to 60 ± 5.1%, with a substantial rise of H_2 to 24 ± 3.8%. This decrease in the FE of HCOOH at a more negative potential indicates dominance of H_2 over HCOOH, as demonstrated by the product distribution (Fig. S19).

To further validate the enhanced catalytic CO_2R activity and active site number, the double-layer capacitance (C_{dl}) principle was employed in the non-Faradaic region to measure the electrochemical surface area (ECSA). Linear fitting of the cyclic voltammetry curves at varied scan rates indicated that the C_{dl} of Sn-Bi_2O_3 at 2.23 mF cm^{-2} (Fig. S20a, c), which is notably higher than Bi_2O_3 (0.76 mF cm^{-2}) (Fig. S20d, c). The calculated ECSA results indicate that the Sn-Bi_2O_3 demonstrates a three times higher active surface area than Bi_2O_3. This increase in ECSA is associated with the decoration of Sn onto Bi_2O_3, which improves catalytic active sites. To further verify the catalytic performances, the partial current densities (j) at various potentials were analyzed (Fig. S21a). The highest j_{HCOOH} of 33.6 ± 1.2 mA cm^{-2} was observed with Sn-Bi_2O_3, 1.5 times that of Bi_2O_3 (22.4 ± 1.6 mA cm^{-2}). A comparison analysis of this study with earlier reported Bi-based catalysts towards HCOOH is summarized in Table S3. Moreover, electrochemical impedance spectroscopy (EIS) was investigated to validate the charge transfer process. Detailed insights are provided through Nyquist plots and equivalent electronic circuits (inset), as depicted in Fig. S21b. Notably, the Nyquist plots demonstrated a charge transfer resistance (R_{ct}) for Bi_2O_3 at 4.13 Ω, which was further reduced to 2.17 Ω for Sn-Bi_2O_3. These EIS outcomes support the accelerated faradic process in EC-CO_2RR, indicating an enhanced capability of hydrated CO_2 molecules to accept electrons, thus readily forming $CO_2^{\bullet-}$ intermediates. The Sn-Bi_2O_3 potentially strengthens electrical conductivity, facilitating faster charge transfer at the catalyst surface and reducing impedance. This leads to a product distribution towards HCOOH, which is associated with a rise in current density under the same potential conditions. The decreased adsorption at more negative potential is further confirmed through CO_2 adsorption studies (Fig. 22a). Isotherms substantiate the superior adsorption capacity of Sn-Bi_2O_3 (0.192 ± 0.05 mmol g^{-1}) than Bi_2O_3 (0.118 ± 0.03 mmol g^{-1}). Moreover, Tafel slope analyses shed light on the reaction kinetics of CO_2RR to validate the selectivity towards HCOOH (Fig. 22b). The low Tafel slope for Sn-Bi_2O_3 NCs at 141 ± 1.7 mV dec^{-1} is lower than the Bi_2O_3 (223 ± 3.3 mV dec^{-1}), implies a faster conversion of CO_2 to HCOOH. The determined slope for Bi_2O_3 indicates that the chemical rate-limiting step entails the primary electron transfer. It is important to note that Tafel slopes increase towards more negative potentials, likely attributed to mass-transport restrictions.

Morphological, crystal and electronic structure analyses

Using micro- and spectroscopic techniques, the morphology of Bi_2O_3 nanosheets (NSs) and Sn-Bi_2O_3 NCs were characterized first. Scanning electron microscopy (SEM) image reveals the flower-like vertical growth of Bi_2O_3 NSs with uniform thickness (Fig. 4a). However, no noticeable morphological alteration was observed by SEM when Sn was incorporated over the Bi_2O_3 NSs (Fig. 4b). Further, the HAADF-STEM image of Bi_2O_3 NSs displays the flower-like morphological structure of the NSs. Subsequently, while characterizing the Sn-Bi_2O_3 NCs, Sn with uniform distribution was observed over Bi_2O_3 NSs (Fig. 4c, d). Further, Energy-Dispersive spectroscopy (EDS) was

https://doi.org/10.1038/s41467-024-51088-0

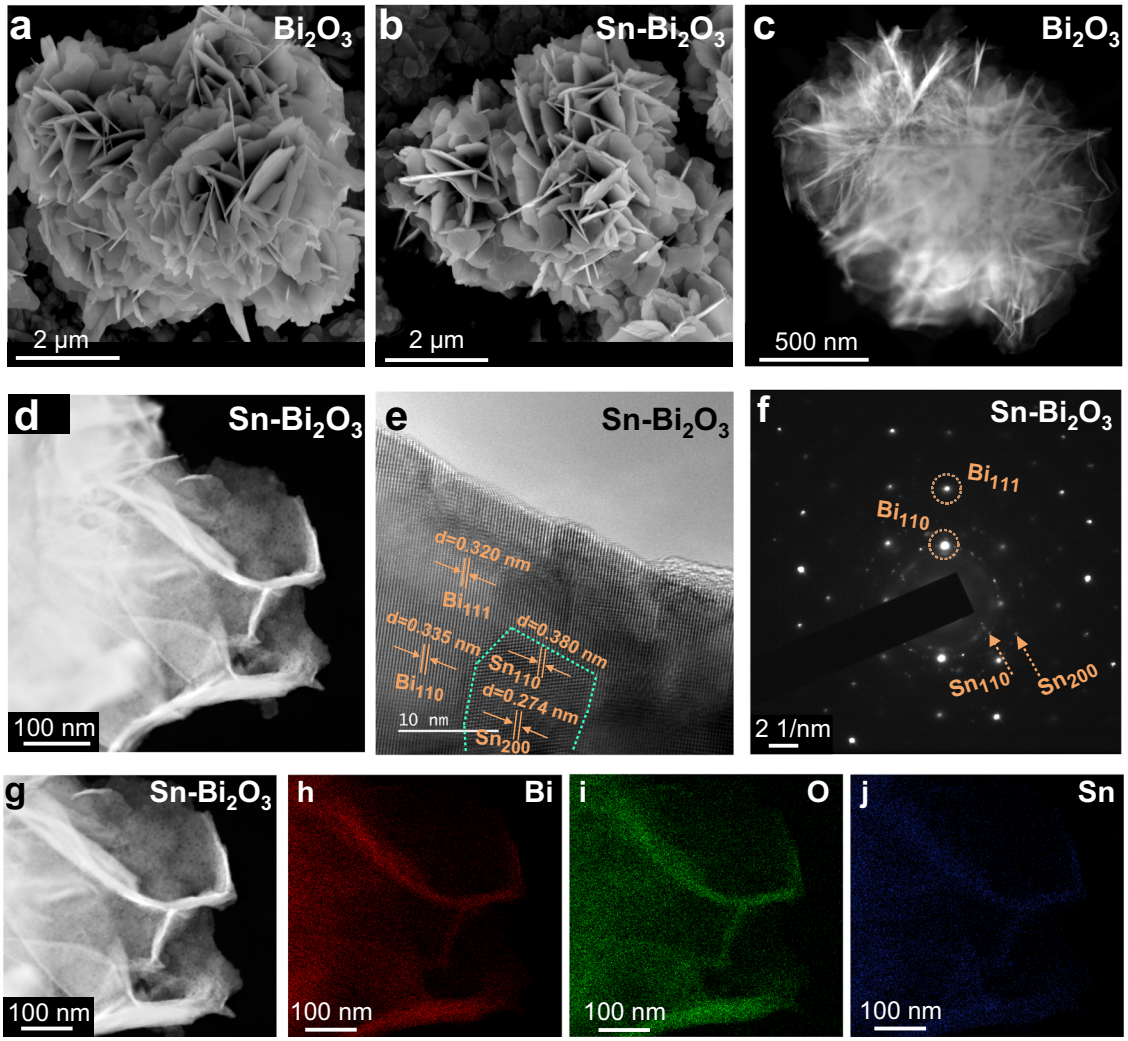

Fig. 4 | Morphological studies of Bi_2O_3 NSs and Sn-Bi_2O_3 NCs. a Field emission scanning electron microscopy images (FE-SEM) of pristine Bi_2O_3 NSs and (**b**) Sn-Bi_2O_3 NCs. **c**, HAADF-STEM images of Bi_2O_3 NSs and **d** Sn-Bi_2O_3 NCs. **e** High-resolution TEM image of Sn-Bi_2O_3 NCs. **f** The selected area electron diffraction pattern (SAEED) of Sn-Bi_2O_3 for Bi and Sn planes. **g**–**j** HAADF-STEM image of Sn-Bi_2O_3 NCs and elemental mapping of Sn, Bi, and O, respectively.

performed in conjunction with HAADF-STEM to reveal the elemental distribution of the Sn, confirming homogenous distributions of Bi, O, and Sn elements in Sn-Bi_2O_3 (Figs. 4g–j and S23a–c). The Bi_2O_3 NSs exhibit a consistent layered morphology before and after Sn modification, as confirmed via TEM, favouring the appropriate exposure of active sites to perform CO_2RR (Fig. S23d–e). Furthermore, the High-Resolution TEM (HRTEM) image of Bi_2O_3 NSs reveals lattice fringes with d-spacings of 0.380 and 0.320 nm, assigned to Bi(110) and Bi(111) facets (Fig. S24), in agreement with the X-ray diffraction (XRD) pattern. In the HRTEM image of Sn-Bi_2O_3 NCs, the interplanar distances of 0.335 and 0.274 nm relate to the Sn(110) and Sn(200) facets, with spacings of 0.380 and 0.320 nm associated with Bi(110) and Bi(111) planes, respectively (Fig. 4e). Selected-area electron diffraction (SAED) patterns were examined to validate the structural properties of Bi_2O_3 NSs and compositionally fine-tuned Sn-Bi_2O_3 NCs. Crystal lattices with Bi(110) and Bi(111) planes at respective interplanar distances of 0.380 and 0.320 nm (Figs. 4e and S24 insets) and Sn(110) and Sn(200) planes at respective d-spacings of 0.335 and 0.274 nm (Fig. 4f) was confirmed through SAED pattern in Sn-Bi_2O_3 NCs.

Moreover, the crystal structure of synthesized Bi_2O_3 NSs and Sn-Bi_2O_3 NCs was investigated using XRD. The sharp diffraction peaks of Bi_2O_3 align with the standard cubic pattern of Bi_2O_3 NSs (JCPDS no. 27-0052, Fig. S25)[44]. However, in the Sn-Bi_2O_3 pattern, no Sn-containing crystalline phases were detected, possibly attributable to the low Sn concentration or the superposition of broad peaks, indicating that Sn modification does not disrupt the crystal structure of Bi_2O_3. Moreover, X-ray photoelectron spectroscopy (XPS) was performed to investigate the catalysts' electronic structure, phase compositions, and valence states. The Bi 4f spectrum of Bi_2O_3 displays two significant peaks relating to Bi $4f_{5/2}$ and Bi $4f_{7/2}$ at 164.11 and 158.88 eV, which confirms negative shifts of 0.16 eV in the binding energy of Sn-Bi_2O_3 NCs, verifying electron transfer, which modulates electronic structures (Fig. 26a). The Bi_2O_3 also displayed an O 1s spectrum with two distinct peaks corresponding to the lattice oxygen in Bi–O bonds and on the adsorbed surface at 530.35 and 531.41 eV; thus, a negative shift of ~0.17 eV in the O 1s peak was observed in the Sn-Bi_2O_3 (Fig. S26b). The commercial metallic Sn displays two Sn^0 corresponding peaks of $3d_{3/2}$ and $3d_{5/2}$ at 493.63 and 485.05 eV, and compared to this, positive shifts of 0.31 eV in the binding energies of Sn^0 with a noticeable change in peak shapes are observed in Sn-Bi_2O_3 NCs (Fig. S26c). This positive shift in the Sn^0 peaks authenticates its partial oxidation, confirming an electron interaction between Sn and Bi_2O_3. Overall, a noticeable downshift in the binding energies of Bi 4f, O 1s and an obvious upshift in Sn 3d confirms electron transfer from Sn to Bi_2O_3 due to the difference in electronegativities, indicating charge redistribution, thereby improving the CO_2R rate. Finally, the survey spectra verify the

presence of Sn, Bi, and O in the Sn-Bi_2O_3 and Bi and O in Bi_2O_3 (Fig. S26d).

Significance of Sn on charge transfer modulation

For better performance, adjusting the work function by increasing the number of electronic states near the Fermi level is essential for semiconductors. With this objective, metallic Sn was interfaced with semiconducting Bi_2O_3 to tune catalytic conversion efficiency. At first, the Mott-Schottky analyses for pristine Bi_2O_3 and Sn-Bi_2O_3 NCs were investigated, which displayed negative slopes, indicating their p-type semiconducting nature (Fig. S27a). The analysis further revealed that the flat band potential of Sn-Bi_2O_3 NCs was calculated at −0.187 V, notably higher than the −0.279 V value measured for Bi_2O_3. To further understand the influence of electronic structure modulation, contact potential difference (V_{CPD}) and the work function (Φ), pivotal factors in composites' interfacial charge transfer dynamics were further investigated using kelvin probe force microscopy (KPFM). The KPFM analysis revealed that metallic Sn demonstrates a lower V_{CPD} of −0.180 mV than the 330 mV value measured for the Bi_2O_3, resulting in the Φ of 4.93 eV for Bi_2O_3 relatively higher than metallic Sn at 4.42 eV (Fig. S27b, Eq. 12)[45,46]. This discrepancy in Φ confirms that Sn possesses a lower electronic Fermi level relative to Bi_2O_3, which can facilitate charge transfer through metal-semiconductor interactions. The KPFM measurements further indicated that metal-semiconductor interfaced Sn-Bi_2O_3 NCs exhibited a V_{CPD} of 70 mV (Fig. S27b). This deviation in the V_{CPD} of Sn-Bi_2O_3 indicates alterations in the work function compared to the Bi_2O_3, predominantly attributed to the charge transfer between metal-semiconductor interfaces. Subsequently, using the V_{CPD} value, the Φ of Sn-Bi_2O_3 was recorded to be 4.67 eV, which is comparatively lower than Bi_2O_3 (Fig. S27c, Eq. 12). This adjustment in Φ generates an electric field at the interfaces that drive charge carrier separation at their contact layers (Fig. S27b). This favorable band alignment promotes efficient electron transfer from Sn to Bi_2O_3, enhancing the electron density at the semiconductor interface, which is advantageous for CO_2RR. Notably, the Sn-Bi_2O_3 NCs modulate charge transfer capabilities relative to pristine Bi_2O_3, facilitating local junction characteristics that align well with Mott-Schottky analysis outcomes (Fig. S27b). The impedance analysis matches well with these findings, which shows that Sn-Bi_2O_3 has reduced charge transfer resistance compared to Bi_2O_3, indicating superior charge transfer kinetics for CO_2RR (Fig. S22b). The measured electronic properties and band alignments for Sn-Bi_2O_3 and Bi_2O_3 are comprehensively summarized in Table S4.

Computational studies

This study further investigated the density functional theory (DFT) calculations to validate the experimental findings. At first, the Gibbs free energy calculation via HCOO* and OCHO* pathways are examined separately to validate how Sn modification affects Bi_2O_3 during HCOOH formation. During CO_2RR, the CO_2 molecule first adsorbed over the catalyst surface, thereby reducing into $CO_2^{\bullet-}$ and converting into the HCOO*/OCHO*. During the initial protonation, carbon atoms of HCOO*/OCHO* bond with the O-bidentate atom on the catalyst surface by positioning the protonated hydrogen atom upwards, whereas oxygen atoms are bonded with either Bi or Sn surface atoms. During the HCOO* conversion pathway, the required formation energy of Sn-Bi_2O_3 reduced from 2.20 eV to 1.45 eV at the Sn site and 0.91 eV at the Bi sites compared to the Bi_2O_3, presenting notable energy differences (ΔE) of 0.75 eV at the Sn sites and 1.29 eV at the Bi sites (Fig. S28a). Conversely, through the OCHO* pathway, the formation energy of Sn-Bi_2O_3 lowers from 1.48 to 1.15 eV at the Sn sites and 0.61 eV at the Bi sites, demonstrating ΔE of 0.87 eV on the Bi site and 0.34 eV on Sn site (Fig. S29a). This initial protonation reaction validated a significant Gibbs free energy difference (ΔG) between Bi_2O_3 and Sn-Bi_2O_3, validating Bi-site in Sn-Bi_2O_3 favorable for HCOO* or OCHO* formation. Notably, these significant energy barriers in HCOO* and OCHO* formation validate the initial proton-coupled electron transfer as a possible rate-limiting step, consistent with Tafel slope observations (Fig. S22b). Subsequently, in the second protonation of HCOO*/OCHO* on its oxygen atom, these adsorbed species react with an electron-proton pair to form stable HCOOH* with a notable decrease in ΔE from the catalysis surface. Overall, the higher ΔE on the Sn-Bi_2O_3 surface confirms the species' favorable formation due to alterations in the electronic structure after Sn modification. Consequently, bonds of HCOO* or OCHO* with HCOOH* are cleaved due to intrinsic scaling relation limitations when Bi_2O_3 is modified with Sn[47]. Overall Gibbs energy calculation results confirm CO_2 to HCOOH conversion via the OCHO* pathway more favorable than HCOO*, as the HCOO* path demands a higher potential, leading to a thermodynamically challenging reaction.

To further ensure the conversion of CO_2 to HCOOH, the adsorption energy of HCOO* and OCHO* on the catalyst surface was examined (Figs. S28b and S29b). For the HCOO* intermediate, the Bi-site of Sn-Bi_2O_3 exhibits a higher adsorption energy of −3.83 eV compared to its Sn-site (−4.39 eV) and the Bi-site (−5.59) of Bi_2O_3. Similarly, for the OCHO* intermediate, the Bi-site of Sn-Bi_2O_3 demonstrates more substantial adsorption energy of −3.14 eV than its Sn-site (−3.40 eV) and the Bi-site of Bi_2O_3 (−4.79 eV). Findings confirm that the negative adsorption energy of HCOO* and OCHO* are favorable for HCOOH formation at the Bi and Sn sites of Sn-Bi_2O_3 relative to Bi_2O_3, confirming facile adsorption and desorption during HCOOH formation. To further gain deeper insight into the root cause of favorable adsorption energies on the Sn-Bi_2O_3 surface, p-projected density of states (p-DOS) analyses via HCOO* and OCHO* paths were performed (Fig. S30a, b). Following both the HCOO* and OCHO* adsorption, the p-DOS of Sn-Bi_2O_3 compared to Bi_2O_3 shifts towards the Fermi level (E_f), confirming the stronger binding affinity to HCOO* and OCHO*. However, the p-DOS associated with OCHO* adsorption analysis reveals a higher E_f than HCOO*, thereby validating that OCHO* exhibits superior binding affinity over the HCOO*. Moreover, a significant upward shift in the E_f of the p-DOS of the Bi and Sn sites in Sn-Bi_2O_3 is observed via OCHO* and HCOO* intermediates. This alteration causes an increase in the antibonding state and decreases the bonding states, resulting in a stronger binding affinity towards intermediates[48]. Hence, an effective HCOOH yield is associated with a shift in adsorption energy and the synergistic effect of Sn and Bi_2O_3. These computed DOS findings agree with the Gibbs free energy simulation outcomes. This is the case even at a high negative potential range; CO_2 and consecutive intermediates possess adequate adsorption capabilities on the catalyst surface.

Post-reaction characterizations

The TEM, XRD, and XPS analyses of the 100 h post-reacted Sn-Bi_2O_3 NCs were conducted to investigate the alterations in surface morphology, structural properties, and chemical state. The post-electrolysis morphological characteristics of Sn-Bi_2O_3 NCs were examined using TEM and HRTEM. Post-reaction TEM analysis shows that the catalyst's surface maintains its initial NSs morphology significantly. However, a notable alteration in the shape of the post-reacted sample's NSs is observed, where initial smooth NSs demonstrate a rougher shape. This morphological transformation is likely a result of surface reconstruction processes occurring within the catalyst during the electrolysis period[49]. Moreover, the HRTEM analyses show that Bi_2O_3 partially reduced to metallic Bi while the core retained its original state (Fig. S31a, b). However, Sn undergoes oxidation while partially retaining its metallic state. Observing the consistent selectivity trends in the initial and final hours of CO_2RR, it is estimated that the number of accessible active sites per electrode area primarily influences the partial variation in overall electrode activity. These structural arrangements maintain the CO_2 reactants and by-products through their active sites. Moreover, the XRD analysis of the 100 h

post-reacted catalyst is characterized, in which diffraction patterns revealed the conversion of the Bi_2O_3 into the $Bi_2O_2CO_3$ phase, consistent with JCPDS No. 41-1448 (Fig. S32)[50]. The emergence of the $Bi_2O_2CO_3$ phase is attributed to aqueous electrolyte-mediated conversion by reaction with HCO_3^- of $KHCO_3$ electrolyte[51]. This factor plays a pivotal role in influencing the CO_2 conversion pathway, featuring the critical impact of electrolyte conditions on the reaction mechanism[50]. These XRD results highlight that the $Bi_2O_2CO_3$ does not compromise the catalyst's fundamental core structure, affirming its stable crystal structure during long-run CO_2RR. Following 100 h of post-CO_2RR, XPS analysis of the Bi 4f spectrum of the post-reacted Sn-$Bi_2O_2CO_3$ catalyst presented two distinct peaks corresponding to Bi $4f_{5/2}$ and Bi $4f_{7/2}$, which validate the presence of Bi^{3+} (Fig. S33a). Simultaneously, in the post-reacted catalyst, the rise of two additional energy peaks at 161.2 and 156.5 eV attributed to Bi $4f_{5/2}$ and Bi $4f_{7/2}$ confirms the formation of metallic Bi^0 (Fig. S33a), consistent with reported literature[52]. The dominant presence of the Bi^{3+} peak in the post-reacted catalyst indicates partial conversion to the metallic Bi^0. In the subsequent analysis, the O 1s spectra of the post-treated sample demonstrated a higher oxygen concentration than the pre-treated sample, indicating increased oxygen adsorption (Fig. S33b). This rise of the additional oxygen peak is attributed to the CO_3^- formed when the Bi_2O_3 reacts with aqueous HCO_3^- and is converted into the $Bi_2O_2CO_3$. Subsequently, in the post-reacted Sn-Bi_2O_3, Sn species exhibited oxidation, with valence states ranging from Sn^0 to Sn^{+4}, further authenticating electronic interactions between the Sn and the Bi_2O_3 (Fig. S33c). This observation confirms that the strong interfacial interaction between Sn and Bi_2O_3 causes a significant alteration in the material's electronic structure. Despite the partial conversion of Bi^{3+} to Bi^0 and Sn^0 to Sn^{4+}, the retention of peaks corresponding to both Bi^{3+} and Sn^0 at their respective positions confirms the structure's integrity of the 100-h post-reacted catalyst. Overall, the post-morphology, crystal structure, and chemical states remain intact except for the change of the crystal phase, partial transitions of Bi^{3+} to metallic Bi, and oxidation of Sn^0. Furthermore, this partial conversion does not hinder the catalyst's durability and selectivity towards HCOOH, aligning with findings reported during CO_2RR[50,52–55]. Post-reaction ECSA was performed further to confirm the electrocatalytic active sites. The cyclic voltammetry curves, linearly fitted at various scan rates, showed that the C_{dl} value for Bi_2O_3 NSs post-reaction was recorded at 0.68 mF cm^{-2}, which slightly decreased from its pre-reaction value of 0.76 mF cm^{-2} (Fig. S20a–c). In contrast, the Sn-Bi_2O_3 NCs also preserved their ECSA performance after reaction and recorded C_{dl} at 2.11 mF cm^{-2}, which is minimally below the pre-reaction value of 2.23 mF cm^{-2} (Fig. S20d–f). These post-reaction ECSA results show that catalysts maintained their ECSA performance with a minimal decrease in the active surface area during 100 h of continuous operation. However, this slight decrease in ECSA can be associated with blocking some active sites owing to the strong adsorption of some contaminants onto the catalyst surface. These post-reaction measurements indicate that Bi_2O_3 and Sn-Bi_2O_3 maintain their catalytic durability and are consistent with post-reaction morphological and chemical state results.

Catalytic reconstruction mechanism

Based on the post-reaction findings, a catalytic reconstruction mechanism is proposed (Figs. S34–S35). During CO_2RR, when Bi_2O_3 were immersed into the 0.5 M aqueous $KHCO_3$ electrolyte, the HCO_3^- ions reacted with catalysts, which underwent an electrolyte-mediated transition and reconstructed a metastable $Bi_2O_2CO_3$ phase as confirmed by XRD analyses (Fig. S32). Further, during CO_2RR, when a negative potential is applied to the Sn-Bi_2O_2, a partial conversion from Bi^{3+} to metallic Bi^0 in the post-reacted sample is confirmed by XPS analysis (Fig. S33). Subsequently, oxidation in the Sn species of the post-reacted sample, with valence states ranging from Sn^0 to Sn^{+4}, was further confirmed. These transitions confirm strong electron coupling between Sn and Bi_2O_3, which promotes electron transfer at their interfaces and changes the electronic structure of active sites, thereby improving the CO_2 conversion rate. During CO_2RR, the reaction environment and negative applied potential are the main driving forces to phase and valance state conversions. Overall, the conversion of Bi_2O_3 into the $Bi_2O_2CO_3$ phase and partial conversion to metallic Bi with oxidation of Sn^0 do not affect the post-reacted catalyst's core structure.

Discussion

This study demonstrates an artificial photosynthesis-inspired unassisted PEC-CO_2RR system design and catalyst engineering approach to convert CO_2 into high-energy density, storable, and economically viable liquid HCOOH. In the devised two-electrode PEC-CO_2RR assembly, a 3-J|Ni/RuO_x-photoanode with Sn-Bi_2O_3-cathode is executed to catalyze the cathodic reduction and anodic oxidation. Under AM 1.5 G irradiation, the unassisted two-electrode CO_2R_{cat}||3-J|Ni/RuO_x setup exhibited an average FE of 88% with 17.3 mmol L^{-1} h^{-1} production rate, leading to a remarkable 12% η_{STF} with 57% of η_{EE} for 100 h operation. In this significant CO_2R performance, the metal-semiconductor interface formation between Sn and Bi_2O_3 cathode-catalyst played a significant role in electronic structure bridging. Subsequently, due to the difference in work functions, metallic Sn transfers electrons to semiconducting Bi_2O_3, which modulates the electronic properties of Sn-Bi_2O_3 NCs. Subsequently, this metal-semiconductor formation generates an electric field at Sn and Bi_2O_3 interfaces, resulting in upshifting in the Fermi level and facilitating charge separation. This favorable band alignment between Sn and Bi_2O_3 leads to a redistribution of electron density, promoting electron transfer from Sn to Bi_2O_3 and facilitating the CO_2 conversion rate. The XPS analyses further confirm an obvious downshift in the binding energies of Bi 4f, with a noticeable upshift in Sn 3d confirming electron transfer from Sn to Bi_2O_3, indicating charge redistribution. These modulations in the electronic structure and increased catalytic active sites in Bi_2O_3 after Sn-loading confirmed significant CO_2 conversion efficiency. The DOS findings further confirm that Sn loading over Bi_2O_3 upshifts the Fermi level. These upshifts in the Fermi level validate a stronger binding affinity between adsorbed species and the catalyst's active sites, thereby facilitating efficient HCOOH formation. The Gibbs free energy calculations further confirm that Sn-Bi_2O_3 NCs reduce the activation energy barrier compared to the Bi_2O_3 surface, strengthening the electronic structure after Sn incorporation. Overall, the devised unassisted PEC setup and catalyst interface engineering approach provide significant insights, including rational design, intrinsic activity, selectivity, and long-run durability, paving the way to synthesize high-energy-density liquid fuels for scalable operations.

Methods

Catalyst preparation

To initiate the synthesis process of Bi_2O_3 NSs, 1.455 g of Bismuth (III) nitrate pentahydrate ($Bi(NO_3)_3{\cdot}5H_2O$) was precisely added into 22.5 mL of ethylene glycol and 51 mL of ethanol. The homogeneous mixture was subjected to ultrasonication and stirring to ensure uniform dispersion of particles and subsequently heated in the autoclave at 160 °C for 5 h. The resultant powder was precisely rinsed and dried overnight in a vacuum to remove residual moisture. Subsequently, the Sn-Bi_2O_3 NCs were synthesized by dispersing the as-prepared Bi_2O_3 NSs into 1 mL of 3 M hydrochloric acid (HCl) and 20 mL of deionized (DI) water. Tin(ii) chloride dihydrate ($SnCl_2.2H_2O$) was then incorporated into the solution with a precise weight percentage ranging from 1 to 4 wt.% of Sn, i.e., for 1% = 0.0199 g, 2% = 0.038, 3% = 0.057 g, 4% = 0.076 g, respectively. Following sonication to obtain a uniform distribution of Sn, the mixture was incrementally transferred into a 10 mL solution of 10 mmol Sodium borohydride ($NaBH_4$) and then stirred to ensure a consistent, homogeneous distribution under Argon gas

environment. Finally, purification with DI water is carried out to eliminate any unreacted species that might still be present in the solution.

Atomic-layer growth of RuO_x

The Atomic Layer Deposition (ALD) of the RuO_x on Ni-foil was executed using an Oxford Instrument Plasma-ALD System. Bis(ethylcyclopentadienyl)ruthenium (II) ($Ru(EtCp)_2$, and oxygen (O_2, 99.999%) utilized as precursors. High-purity Argon (Ar, 99.999%), utilized as a purge gas, and oxygen (O_2, 99.999%) as a carrier gas, were supplied throughout the deposition. The Ni-foil affixed to the silicon substrate was subsequently loaded into the reactor chamber. Notably, the chamber temperature was maintained at 270 °C, while the $Ru(EtCp)_2$ precursor was kept at a steady 110 °C, thereby providing a constant flux of Ru to the reactor. Meanwhile, the gas line temperature was fixed at 150 °C to prevent precursor condensation. The deposition protocol entailed a 1-second $Ru(EtCp)_2$ pulse and a 5-second oxygen pulse, each followed by a 20-second Argon purge. Modulation of deposition, including density, size, and distribution, was achieved through adjustments to the number of processing cycles.

Fabrication of photoanode

The 3-J|Ni/RuO_x photoanode was precisely fabricated by applying the silver paste to the Ge side of the solar cell (InGaP/GaAs/Ge), serving the dual purpose of creating an ohmic contact and furnishing an adhesive layer. This was successively followed by incorporating a compact RuO_x-deposited Ni-foil, precisely measuring 1 × 1 cm^2, as elucidated in the Atomic-layer deposition of RuO_x above. This inclusion functions as a protective barrier and an oxidation layer under aqueous environmental conditions. Post to this integration, insulation of the backside was achieved using epoxy, ensuring that the catalyst layer was explicitly exposed to the anolyte, thereby facilitating water oxidation. Furthermore, on the front top finger of the photoelectrode, the ohmic contact was proficiently accomplished by leveraging a Ga-In eutectic alloy. Subsequently, a Copper (Cu) strip, connected via silver paste, was extended to secure the reliable performance measurement throughout the operation. Prior to PEC testing, the epoxy and adhesive layers were subjected to vacuum drying at a temperature of 70 °C for 1 h. The individual 3-J|Ni/RuOx photoanode image is presented in Fig. S36a.

Preparation of CO_2 reduction electrode

The cathode electrode was fabricated by adding 5 mg of the pre-synthesized CO_2R catalyst into a mixture of 0.7 mL of ethanol, 0.3 mL of deionized (DI) water, and 10 μL of Nafion solution. This solution underwent sonication for 1 h to ensure uniform dispersion. The 100 mL resulting catalyst ink was taken and precisely drop-casted onto 1 × 1 cm^2 carbon paper. The mass loading of the CO_2RR catalyst was measured to 0.51 ± 0.07 mg cm^{-2}. Following vacuum drying, the treated carbon paper was employed as the cathode electrode during CO_2RR. The photograph of the cathode electrode with catalyst loading over carbon paper is illustrated in Fig. S36b.

Electrochemical and photoelectrochemical analyses

The corresponding EC and PEC experiments were employed with Zahner Zennium Pro potentiostat. All presented cell voltage measurements for EC and PEC have not been corrected by internal resistance (iR). The PEC and electrochemical reactions were performed in a two-compartment setup equipped with a bipolar membrane to inhibit generated products and electrolyte crossover. Prior to use, the bipolar membrane (fumasep® FBM) was soaked in 0.5 M NaCl solution for 24 h and then preserved at room temperature in 0.5 M NaCl aqueous solution. Before using it in EC and PEC setup, it was cut into 3.0 × 3.0 cm^2 and rinsed with DI water. Moreover, the reactions were conducted with 0.5 M KOH anolyte and 0.5 M $KHCO_3$ catholyte in the aqueous conditions. The pH value from ten separate measurements was recorded, which is 14.0 ± 0.023 for 0.5 M KOH and 7.4 ± 0.017 for 0.5 M $KHCO_3$, respectively. Using an electrochemical workstation, the resistance of the electrochemical cell was measured and recorded at 2.14 ± 0.013 Ω. Prior to testing, the cathodic chamber was purged with CO_2 or Ar. gases for 30 min to create pre-gas-saturation, and 10 sccm flow rate was maintained during the experiment.

Initially, an evaluation of the EC performance of the anode and cathode at varying applied potentials was conducted to confirm the selectivity of yielded products and operational potential. The three-electrode setup, which comprised a Bi_2O_3 and Sn-Bi_2O_3 catalysts working, Pt-mesh counter, and Ag/AgCl reference electrodes, facilitated this process. After this, the electrochemical measurements of Ni/RuO_x, acting as an oxidation catalyst, were further scrutinized in a three-electrode configuration to authenticate the operating potential. Furthermore, it is noteworthy that all potentials calculated experimentally during the EC processes were referenced to the reversible hydrogen electrode (RHE) from Ag/AgCl, as per Eq. (1).

$$E_{RHE} = E_{(Ag/AgCl)} + 0.197 + 0.059 \times pH \tag{1}$$

The EC measurements were performed in the three-electrode setup, using cathode (Bi_2O_3 or Sn-Bi_2O_3)-catalysts−working, Ag/AgCl−reference and Pt-foil anode−counter electrodes, respectively. All EC measurements were conducted within the CO_2-saturated conditions. The electrochemical impedance spectroscopy (EIS) measurements were assessed at −0.8 V within 0.5 M $KHCO_3$ solution, employing a 5 mV amplitude across a frequency spectrum from 1 Hz to 10000 Hz. A Tafel plot illustrating overpotential versus the log j_{HCOOH} was generated from the results of controlled potential electrolysis. Moreover, PEC-CO_2RR was executed in three- and two-electrode configurations under 1-sun illumination. In a three-electrode setup, the 3-J|Ni/RuO_x photoanode, Sn-Bi_2O_3 cathode and Ag/AgCl reference electrodes assisted this PEC operation. However, the 3-J|Ni/RuO_x−photoanode and Sn-Bi_2O_3−cathode were the requisite electrodes in the two-electrode setup. All PEC reactions were conducted under 1-sun illumination at ambient conditions, complemented by continuous magnetic stirring. The ensuing photocurrents were subsequently normalized to the photoactive area of the 3-J|Ni/RuO_x photoanode. The SS-X Solar simulator with the solar filter of AM 1.5 G served as a light source. Prior to initiating PEC measurements, the light intensity was precisely regulated at 100 mW cm^{-2}. For both the two- and three-electrode "Counter Electrode Potential" measurements, Zahner Zennium Pro potentiostat was employed. For performing three-electrode configured "Counter Electrode Potential" measurements, a 3-J|Ni/RuO_x photoanode−working with Ag/AgCl−reference electrode in the anodic chamber, and the Sn-Bi_2O_3 catalyst−counter electrode in the cathodic chamber was executed. Subsequently, during two-electrode "Counter Electrode Potential" quantification, 3-J|Ni/RuO_x photoanode−working without a reference electrode in the anodic chamber, and Sn-Bi_2O_3 catalyst−counter electrode in the cathodic chamber was employed.

In addition, the external quantum efficiency (EQE) was quantified using the QE-R monochromator system, represented by Eq. (2). Here, 'h' is the Planck Constant, 'c' is the speed of light, 'J' is the photocurrent density, 'e' is the electronic charge, 'λ' represents the wavelength, and 'Pλ' is the flux of light intensity dependent on wavelength.

$$EQE(\%) = \frac{hcj}{e\lambda P_\lambda} \tag{2}$$

Further, the solar-to-fuel conversion efficiency (η) for the various CO_2R products obtained was calculated using Eq. (3). In this context, 'J_{op}' signifies the operational current, 'E°' is the thermodynamic potential of the chosen product (for HCOOH, −0.17 V vs RHE), and

'FE' denotes the Faradaic efficiency.

$$\eta_{STF}\% = \frac{J_{op} \times \left[1.23V - E^{\circ}\right] \times FE}{100mW.m^{-2}} \quad (3)$$

Additionally, solar-to-hydrogen conversion efficiency (η_{STH}) was quantified via Eq. (4). In the given equation, 'J_{op}' shows the operational current.

$$\eta_{STH}\% = \frac{J_{op} \times 1.23 \times FE}{100mW.m^{-2}} \quad (4)$$

Moreover, the electrical energy efficiency of the products derived during PEC-CO_2RR was determined using Eq. (5). Here, E_{chem} is the energy used for the CO_2 conversion, and $E_{applied}$ is the electrical energy input. Moreover, 'E°' indicates the thermodynamic potential of the cathodic and anodic reactions; for instance, $E^0 = E_{OER} - E_{CO2RR}$. Here, '$E_{OER}$' is 1.23 V vs RHE (anodic potential of water oxidation), and 'E_{CO2RR}' is −0.17 V vs RHE (cathodic potential of HCOOH). 'E_{cell}' represents the total supply voltage generated by solar cells (i.e. 2.2 V in three-electrode and 2.05 V in two-electrode configuration).

$$\eta_{EE} = \frac{E_{chem}}{E_{applied}} = \frac{E^0 \times FE\%}{E_{cell}} \quad (5)$$

Product Quantification

Online gas chromatograph quantitatively facilitated the amount of resultant gaseous products (Agilent 7890 B). Subsequently, the liquid products were quantified via a 600 MHz ^{1}H nuclear magnetic resonance spectroscopy (NMR) to ascertain their constituents. Prior to NMR experimentation, an analytical composition of 500 µl of resultant electrolyte solution, 120 µl D_2O, and 10 µl of a 0.05 mmol L^{-1} DMSO internal standard was integrated into an NMR tube for subsequent analysis. Before generating the ^{1}H spectrum, water signals were attenuated using a pre-saturation methodology, ensuring a more precise assessment of the remaining constituents.

Moreover, the analysis of FE% of HCOOH and hydrogen was determined using Eq. (6), where the number '2' symbolizes the requisite electrons for the formation of either HCOOH or a hydrogen molecule, 'n' signifies the number of total moles in the product, 'F' stands for Faraday constant (96485), and 'Q' corresponds to the cumulative charge supplied by the potentiostat or 3-J photoanode during CO_2RR testing.

$$FE = \frac{2nF}{Q} \times 100\% \quad (6)$$

The production rate during EC and PEC-CO_2RR processes can be comprehensively determined via Eq. (7). In this formula, 'ν_{HCOOH}' symbolizes the concentration of the obtained product, 'C_{HCOOH}' denotes the concentration of HCOOH, 'V' signifies the electrolyte volume used in the reaction, 'S' is indicative of the geometric surface area of the engaged electrolyte, and 't' corresponds to the time duration of the operation.

$$\nu_{HCOOH} = \frac{C_{HCOOH} \times V}{S \times t} \quad (7)$$

Electrochemical surface area measurements

The electrochemical capacitance was investigated further by calculating non-Faradaic capacitive currents related to the C_{dl} to investigate the effect of the number of active sites. This was achieved by analyzing the scan-rate dependency observed in cyclic voltammograms. In the non-faradaic region, a small current arises from surface adsorption-desorption, generating a capacitance at the electrode-electrolyte interfaces, thereby forming double layers. By linearly fitting the variation of peak current density ($J_{pc} - J_{pa}$) against the scan rate, which correlates to the number of active sites in the electrocatalyst. Generally, the higher C_{dl} indicates a strong interaction between the electrolyte and the electrodes, reflecting the number of catalytic centers and providing insights into the ECSA. The ECSA of the electrodes was computed from their C_{dl} values using the given Eq. (8):

$$ECSA = \frac{C_{dl}}{C_S} \quad (8)$$

Here, C_S represents the specific capacitance of the sample, defined as the capacitance per unit area of an atomically smooth planar surface of the material under the same electrolyte conditions. This ECSA calculation uses a general specific capacitance value of $C_S = 0.029$ mF[56].

Computational Details

The computational study deploying Density Functional Theory (DFT) was executed via the Vienna ab initio simulation package[43]. The interaction between valence electrons and ions was proficiently modeled using projector-augmented wave (PAW) potentials. Additionally, the Perdew–Burke–Ernzerhof (PBE) rendition of the Generalized Gradient Approximation (GGA) was utilized to handle the electron exchange-correlation[57]. Notably, van der Waals (vdW) interaction calculations were implemented through the DFT-D3 methodology. A plane wave cutoff energy of 520 eV, with 3 × 3 × 1 sheet k-point mesh for Bi_2O_3 geometry, was implemented to ensure an accurate density of electronic states. The ionic relaxations were conducted under a conventional energy of 10^{-4} eV and convergence criteria force of 0.01 eV/Å. The adjusted lattice parameters for Bi_2O_3 (200) have been determined as $a = 26.77$ Å, $b = 11.77$ Å, and c = 19.36 Å, and this structural configuration of Bi_2O_3 is derived from a single-layer model. To further simulate the influence of Sn in the Sn-Bi_2O_3 catalyst system, a Sn-Bi_2O_3 surface was constructed by incorporating Sn atoms onto the pure Bi_2O_3 (200) surface (Fig. S37). Moreover, a Bi_2O_3 slab mimicked the (200) lattice plane, and a 1.5 nm vacuum layer was employed to prevent interactions with adjacent layers.

Additionally, Gibbs free energies of all adsorbed and gaseous species at 298.15 K were calculated using the expression in the corresponding Eq. (9). Where 'E' signifies the DFT-determined electronic energy for a given geometric structure, 'E_{ZPE}' represents the zero-point energy estimated at the harmonic approximation by the vibrational frequency of a molecule/adsorbate, 'T' stands for temperature, and 'S' denotes entropy.

$$\Delta G = \Delta E_{DFT} - \Delta E_{ZPE} + T\Delta S \quad (9)$$

Within this computational framework, each reaction step in the computational hydrogen electrode (CHE) model was regarded as an instantaneous electron-proton pair transfer through the applied potential. Ultimately, the adsorbate's adsorption energy (E_{ads}) was calculated using Eq. (10).

$$E_{ads} = E_{substrate+adsorbate} - E_{substrate} - E_{adsorbate} \quad (10)$$

Mott-Schottky Analysis

The Admiral Squidstat plus multichannel potentiostats were employed for the Mott-Schottky analysis during flat band potential (V_{fb}) measurements. Under a three-electrode system, this analysis utilized 0.5 M $KHCO_3$ as the electrolyte, a Pt wire as the counter and Ag/AgCl as the reference electrodes. Frequency ranged from 1 Hz to 100 kHz within

the potential range from 0.2 V to −1.0 vs Ag/AgCl. The measurements of V_{fb} were based on the following Mott-Schottky Eq. (11).

$$C^{-2} = \frac{2}{e_0 \varepsilon_0 \varepsilon_0 N_d}(V - V_{fb} - \frac{kT}{e_0}) \quad (11)$$

Where C denotes the electrode surface's space charge layer capacitance, e_0 the electronic charge, ε_O vacuum permittivity, ε_r the dielectric constant, N_d the donor site density, V the applied potential, k the Boltzmann constant, and T the absolute temperature, a plot of C^{-2} vs V (vs RHE) with a negative slope signifies the material's p-type semiconducting characteristic.

Kelvin probe force microscopy (KPFM) analysis

KPFM was conducted to assess the contact potential difference and the material's work function. Utilizing an MFP-3D infinity model atomic force microscopy with a conductive tip in tapping mode, KPFM allowed for probing the work function (Φ in eV), determined from the contact potential difference (V_{CPD} in mV) between the tip and material through a given Eq. (12). Here, the electronic charge (e) is equal to 1.623×10^{-19}.

$$V_{CPD} = \frac{\Phi_{material}(eV) - \Phi_{tip}(eV)}{e} \quad (12)$$

Data availability

All data supporting the findings of this study in the main manuscript and supporting information are provided as a Source Data file and atomic coordinates of the optimized computational model are shared in Science Data Bank (https://doi.org/10.57760/sciencedb.11027). Source data are provided with this paper.

References

1. Köpke, M. Redesigning CO_2 fixation. *Nat. Synth.* **1**, 584–585 (2022).
2. Peter, S. C. Reduction of CO_2 to chemicals and fuels: a solution to global warming and energy crisis. *ACS Energy Lett.* **3**, 1557–1561 (2018).
3. Armstrong McKay, D. I. et al. Exceeding 1.5 °C global warming could trigger multiple climate tipping points. *Science* **377**, eabn7950 (2022).
4. Rahimi, M., Khurram, A., Hatton, T. A. & Gallant, B. Electrochemical carbon capture processes for mitigation of CO_2 emissions. *Chem. Soc. Rev.* **51**, 8676–8695 (2022).
5. Rahaman, M. et al. Solar-driven liquid multi-carbon fuel production using a standalone perovskite–$BiVO_4$ artificial leaf. *Nat. Energy* **8**, 629–638 (2023).
6. Zhang, W., Jin, Z. & Chen, Z. Rational-designed principles for electrochemical and photoelectrochemical upgrading of CO_2 to value-added chemicals. *Adv. Sci.* **9**, 2105204 (2022).
7. Wei, K., Guan, H., Luo, Q., He, J. & Sun, S. Recent advances in CO_2 capture and reduction. *Nanoscale* **14**, 11869–11891 (2022).
8. Kistler, T. A., Um, M. Y., Cooper, J. K., Sharp, I. D. & Agbo, P. Exploiting heat transfer to achieve efficient photoelectrochemical CO_2 reduction under light concentration. *Energy Environ. Sci.* **15**, 2061–2070 (2022).
9. Lv, J. et al. Solar utilization beyond photosynthesis. *Nat. Rev. Chem.* **7**, 91–105 (2023).
10. Antón-García, D. et al. Photoelectrochemical hybrid cell for unbiased CO_2 reduction coupled to alcohol oxidation. *Nat. Synth.* **1**, 77–86 (2022).
11. Zhu, P. & Wang, H. High-purity and high-concentration liquid fuels through CO_2 electroreduction. *Nat. Catal.* **4**, 943–951 (2021).
12. Chatterjee, S., Dutta, I., Lum, Y., Lai, Z. & Huang, K.-W. Enabling storage and utilization of low-carbon electricity: power to formic acid. *Energy Environ. Sci.* **14**, 1194–1246 (2021).
13. Andrei, V. et al. Floating perovskite-$BiVO_4$ devices for scalable solar fuel production. *Nature* **608**, 518–522 (2022).
14. Andrei, V., Reuillard, B. & Reisner, E. Bias-free solar syngas production by integrating a molecular cobalt catalyst with perovskite–$BiVO_4$ tandems. *Nat. Mater.* **19**, 189–194 (2020).
15. Li, D., Yang, K., Lian, J., Yan, J. & Liu, S. Powering the world with solar fuels from photoelectrochemical CO_2 reduction: basic principles and recent advances. *Adv. Energy Mater.* **12**, 2201070 (2022).
16. Zhou, X. et al. Solar-driven reduction of 1 atm of CO_2 to formate at 10% energy-conversion efficiency by use of a TiO_2-protected III–V tandem photoanode in conjunction with a bipolar membrane and a Pd/C cathode. *ACS Energy Lett.* **1**, 764–770 (2016).
17. Liu, B. et al. Back-illuminated photoelectrochemical flow cell for efficient CO_2 reduction. *Nat. Commun.* **13**, 7111 (2022).
18. Roh, I. et al. Photoelectrochemical CO_2 reduction toward multi-carbon products with silicon nanowire photocathodes interfaced with copper nanoparticles. *J. Am. Chem. Soc.* **144**, 8002–8006 (2022).
19. Zhang, Y. et al. Photoelectrocatalytic reduction of CO_2 to syngas via SnO_x-enhanced Cu_2O nanowires photocathodes. *Adv. Funct. Mater.* **32**, 2109600 (2022).
20. Kistler, T. A., Um, M. Y., Cooper, J. K., Sharp, I. D. & Agbo, P. Monolithic photoelectrochemical CO_2 reduction producing syngas at 10% efficiency. *Adv. Energy Mater.* **11**, 2100070 (2021).
21. Li, D., Yang, K., Lian, J., Yan, J. & Liu, S. Powering the world with solar fuels from photoelectrochemical CO_2 reduction: basic principles and recent advances. *Adv. Energy. Materials* **12**, 2201070 (2022).
22. Bhattacharjee, S. et al. Photoelectrochemical CO_2-to-fuel conversion with simultaneous plastic reforming. *Nat. Synth.* **2**, 182–192 (2023).
23. Andrei, V. et al. Long-term solar water and CO_2 splitting with photoelectrochemical BiOI–$BiVO_4$ tandems. *Nat. Mater.* **21**, 864–868 (2022).
24. Khan, M. et al. Importance of oxygen measurements during photoelectrochemical water-splitting reactions. *ACS Energy Lett.* **4**, 2712–2718 (2019).
25. Masel, R. I. et al. An industrial perspective on catalysts for low-temperature CO_2 electrolysis. *Nat. Nanotechnol.* **16**, 118–128 (2021).
26. Yang, S. et al. Halide-guided active site exposure in bismuth electrocatalysts for selective CO_2 conversion into formic acid. *Nat. Catal.* **6**, 796–806 (2023).
27. Xie, C., Niu, Z., Kim, D., Li, M. & Yang, P. Surface and interface control in nanoparticle catalysis. *Chem. Rev.* **120**, 1184–1249 (2019).
28. van Deelen, T. W., Hernández Mejía, C. & de Jong, K. P. Control of metal-support interactions in heterogeneous catalysts to enhance activity and selectivity. *Nat. Catal.* **2**, 955–970 (2019).
29. Biswas, A. et al. Alteration of electronic band structure via a metal–semiconductor interfacial effect enables high faradaic efficiency for electrochemical nitrogen fixation. *ACS Nano* **15**, 20364–20376 (2021).
30. Shi, Y. et al. Electronic metal–support interaction modulates single-atom platinum catalysis for hydrogen evolution reaction. *Nat. Commun.* **12**, 3021 (2021).
31. Li, X. et al. Advances in heterogeneous single-cluster catalysis. *Nat. Rev. Chem.* **7**, 754–767 (2023).
32. Wen, G. et al. Engineering electrochemical surface for efficient carbon dioxide upgrade. *Adv. Energy Mater.* **12**, 2103289 (2022).
33. Wen, G. et al. Orbital interactions in Bi-Sn bimetallic electrocatalysts for highly selective electrochemical CO_2 reduction toward formate production. *Adv. Energy Mater.* **8**, 1802427 (2018).
34. Khan, B. et al. Electronic and nanostructure engineering of bifunctional MoS_2 towards exceptional visible-light photocatalytic CO_2 reduction and pollutant degradation. *J. Hazard. Mater.* **381**, 120972 (2020).

35. Faheem, M. B. et al. All-inorganic perovskite solar cells: energetics, key challenges, and strategies toward commercialization. *ACS Energy Lett.* **5**, 290–320 (2019).
36. Li, Z. et al. Solar Hydrogen. *Adv. Energy Mater.* **13**, 2203019 (2023).
37. Khan, M. A., Al-Shankiti, I., Ziani, A., Wehbe, N. & Idriss, H. A stable integrated photoelectrochemical reactor for H_2 production from water attains a solar-to-hydrogen efficiency of 18% at 15 suns and 13% at 207 suns. *Angew. Chem.* **132**, 14912–14918 (2020).
38. Laskowski, F. A. et al. Nanoscale semiconductor/catalyst interfaces in photoelectrochemistry. *Nat. Mater.* **19**, 69–76 (2020).
39. Zheng, T. et al. Copper-catalysed exclusive CO_2 to pure formic acid conversion via single-atom alloying. *Nat. Nanotechnol.* **16**, 1386–1393 (2021).
40. Fan, L., Xia, C., Zhu, P., Lu, Y. & Wang, H. Electrochemical CO_2 reduction to high-concentration pure formic acid solutions in an all-solid-state reactor. *Nature. Communications* **11**, 3633 (2020).
41. Wang, Q., Pornrungroj, C., Linley, S. & Reisner, E. Strategies to improve light utilization in solar fuel synthesis. *Nat. Energy* **7**, 13–24 (2022).
42. Xing, Y. et al. Bi@Sn core–shell structure with compressive strain boosts the electroreduction of CO_2 into formic acid. *Adv. Sci.* **7**, 1902989 (2020).
43. Wu, Z. et al. Engineering bismuth–tin interface in bimetallic aerogel with a 3D porous structure for highly selective electrocatalytic CO_2 reduction to HCOOH. *Angew. Chem.* **133**, 12662–12667 (2021).
44. Dutta, A. et al. A tandem (Bi_2O_3 → Bimet) catalyst for highly efficient ec-CO_2 conversion into formate: operando raman spectroscopic evidence for a reaction pathway change. *ACS Catal.* **11**, 4988–5003 (2021).
45. Hölzl, J. & Schulte, F. K. Work function of metals. *Solid Surf. Phys.* **85**, 1–150 (2006).
46. Dai, W. et al. Constructing robust Bi active sites in situ on α-Bi_2O_3 for efficient and selective photoreduction of CO_2 to CH_4 via directional transfer of electrons. *ACS Catal.* **13**, 2513–2522 (2023).
47. Li, X. et al. Sn-Doped Bi_2O_3 nanosheets for highly efficient electrochemical CO_2 reduction toward formate production. *Nanoscale* **13**, 19610–19616 (2021).
48. Wu, J. et al. Multivalent Sn species synergistically favours the CO_2-into-HCOOH conversion. *Nano Res.* **14**, 1053–1060 (2021).
49. Wu, D., Huo, G., Chen, W., Fu, X.-Z. & Luo, J.-L. Boosting formate production at high current density from CO_2 electroreduction on defect-rich hierarchical mesoporous Bi/Bi_2O_3 junction nanosheets. *Appl. Catal. B: Environ.* **271**, 118957 (2020).
50. Tran-Phu, T. et al. Nanostructured β-Bi_2O_3 fractals on carbon fibers for highly selective CO_2 electroreduction to formate. *Adv. Funct. Mater.* **30**, 1906478 (2020).
51. Xu, Y. et al. Selective CO_2 electroreduction to formate on polypyrrole-modified oxygen vacancy-rich Bi_2O_3 nanosheet pre-catalysts by local microenvironment modulation. *Small* **19**, 2300001 (2023).
52. Liu, S., Lu, X. F., Xiao, J., Wang, X. & Lou, X. W. Bi_2O_3 nanosheets grown on multi-channel carbon matrix to catalyze efficient CO_2 electroreduction to HCOOH. *Angew. Chem.* **131**, 13966–13971 (2019).
53. Gong, Q. et al. Structural defects on converted bismuth oxide nanotubes enable highly active electrocatalysis of carbon dioxide reduction. *Nat. Commun.* **10**, 2807 (2019).
54. Han, N. et al. Ultrathin bismuth nanosheets from in situ topotactic transformation for selective electrocatalytic CO_2 reduction to formate. *Nat. Commun.* **9**, 1320 (2018).
55. Lee, C. W. et al. Selective electrochemical production of formate from carbon dioxide with bismuth-based catalysts in an aqueous electrolyte. *ACS Catal.* **8**, 931–937 (2018).
56. Zheng, X. et al. Sulfur-modulated tin sites enable highly selective electrochemical reduction of CO_2 to formate. *Joule* **1**, 794–805 (2017).
57. Liu, S.-Q. et al. Electronic delocalization of bismuth oxide induced by sulfur doping for efficient CO_2 electroreduction to formate. *ACS Catal.* **11**, 7604–7612 (2021).

Acknowledgements

This work is supported by the City University of Hong Kong (9380107) and KAUST Catalysis Center, King Abdullah University of Science and Technology.

Author contributions

Bilawal Khan devised the setup, fabricated the PEC device, synthesized the catalysts, and wrote the first draft of the manuscript. M. Bilal Faheem and Jinlan Nie conducted theoretical calculations and wrote the theoretical part. Bilawal Khan and Karthik Peramaiah carried out the EC and PEC measurements and analyzed the experimental data. Hau Huang, Zhongxiao Li and Chen Liu performed product quantification of liquid fuel. Jr-Hau He and Kuo-Wei Huang supervised the project. All authors revised and commented on the manuscript's writing.

Competing interests

All authors declare no competing interests.

Additional information

Supplementary information The online version contains supplementary material available at https://doi.org/10.1038/s41467-024-51088-0.

Correspondence and requests for materials should be addressed to Jr-Hau He.

Peer review information *Nature Communications* thanks Joel Ager III and the other, anonymous, reviewers for their contribution to the peer review of this work. A peer review file is available.